Rodríguez-Zuluaga *et al.*
Earth, Planets and Space (2022) 74:119
https://doi.org/10.1186/s40623-022-01679-2

Earth, Planets and Space

FRONTIER LETTER

Open Access

Topside equatorial spread *F*-related field-aligned Poynting flux: observations and simulations

J. Rodríguez-Zuluaga[1]*, C. Stolle[2], D. Hysell[3] and D. J. Knudsen[4]

Abstract

Electric and magnetic field data from the Swarm constellation mission are used to report on the Poynting flux associated with postsunset topside equatorial spread *F*. A three-dimensional numerical simulation of plasma density irregularities in the *F* region ionosphere leading to spread *F* is used to interpret and support the satellite observations. Here, we focus on quasi-static magnetic and electric fields nearby equatorial plasma depletions (EPDs). The observations show a correlation of the Poynting flux with the plasma number density when background densities are larger than 10^5 cm^{-3}—typical of pre-midnight hours. In other words, the Poynting flux increases as EPDs get more depleted. As time passes, both plasma density and Poynting flux decay. For the latter, however, this temporal dependence is evident in the pre-midnight sector only. Concerning spatial variations, the Poynting flux is observed to enhance inside EPDs as a function of magnetic latitude mainly due to the strengthening of field-aligned currents as they flow away from the dip equator. The Poynting flux follows the dynamo theory, wherein the winds in the *F* region act as the generator at night and the *E* region conductivity on shared magnetic field lines as the load. That said, the Poynting flux is generally expected to flow along the field lines away from a dynamo source at the dip equator. Nevertheless, observations show unidirectional flows from one magnetic hemisphere to another, suggesting a generator below the satellites' altitude. The numerical simulations confirm these observations and show that such latitudinal shifts of the generator are due almost entirely to the winds.

Keywords: Equatorial spread *F*, Plasma density depletions, Poynting flux, Swarm, Spread *F* simulation

---

*Correspondence: juanrz@gfz-potsdam.de

[1] GFZ German Research Centre for Geosciences, Potsdam, Germany
Full list of author information is available at the end of the article

Graphical Abstract

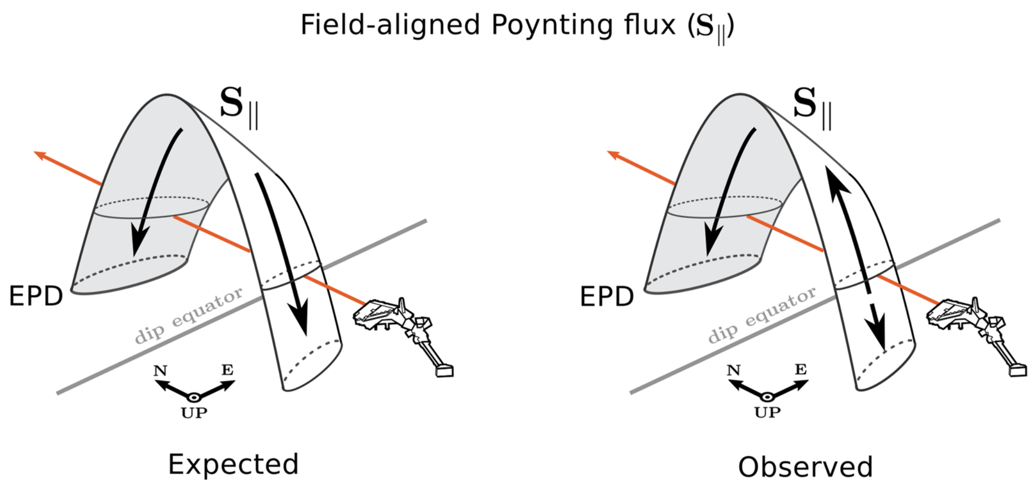

Introduction

The term equatorial spread *F* (ESF) comes from the spreading of ionogram traces initially observed at nighttime by Booker and Wells (1938) at a station near the magnetic equator. Accurately, the authors interpreted these perturbations as radio scattering from plasma density fluctuations. For many years, the name spread *F* was used to label ionograms where the critical plasma frequency could not be read due to this phenomenon. Nowadays, the name is used to refer to the whole spectrum of plasma density irregularities related to ionospheric interchange instabilities in the nighttime equatorial *F* region (Hysell 2000). The wide range of scale sizes of ESF-related plasma irregularities—extending from centimeters to hundreds of kilometers—has allowed studying the phenomenon via coherent and incoherent scatter radars, ionosondes, HF scattering experiments, scintillation measurements, in situ space-based probes, and far-ultraviolet airglow images (Fejer and Kelley 1980; Woodman 2009, and references therein).

Among the different kinds of spread *F*, i.e., bottom-type, bottomside, and topside spread *F*, this study concentrates exclusively on the latter. Topside spread *F* is seen as large-scale plasma density depleted channels aligned with the Earth's magnetic field, also referred to as equatorial plasma depletions (EPDs) or bubbles. EPDs generally present—relative to the ambient plasma and perpendicular to the main magnetic field—large upward vertical drift velocities and eastward zonal electric fields within the depletion which allows the structure to rise, reaching altitudes of about 2000 km or more—sometimes even exceeding the ion-acoustic speed (e.g., Aggson et al. 1992). Due to the strong disruption of the ionospheric equilibrium density profile by EPDs, eastward zonal currents diverge at the walls of EPDs as field-aligned currents. These latter currents grow as a function of magnetic latitude due to current conservation along the magnetic flux tube, as depicted in panels a and b of Fig. 1. Inside the depletion, weak zonal currents build-up to maintain the current continuity through Pedersen and gravity-driven currents. Alfvén waves also contribute to this current system through field-aligned currents and transverse polarization currents as they propagate away from the EPD-related dynamo source while rising (e.g., Aggson et al. 1992; Bhattacharyya and Burke 2000).

The first in situ observational evidence of magnetic fluctuations related to electric currents in the nighttime *F* region were reported by Lühr et al. (2002) using the high-precision magnetometer onboard the CHAMP satellite. Among their results, the authors also identified magnetic fluctuations associated with EPD-related currents—field-aligned and diamagnetic currents, specifically. Although Aggson et al. (1992) pinpointed magnetic perturbations at the edges of EPDs using the DE 2 satellite, these ones were of Alfvénic origin—different to the perturbations reported by Lühr et al. (2002) inside EPDs. Subsequently, the first comprehensive assessment of spread *F* magnetic signatures was documented by Stolle et al. (2006) using 5 years of CHAMP magnetic field data. In their study, the authors used magnetic field perturbations associated with diamagnetic currents to derive a global climatology of EPDs' occurrence. They also deduced the orientation of field-aligned currents (FACs) at the walls of EPDs. Previous studies have described (e.g., Burke

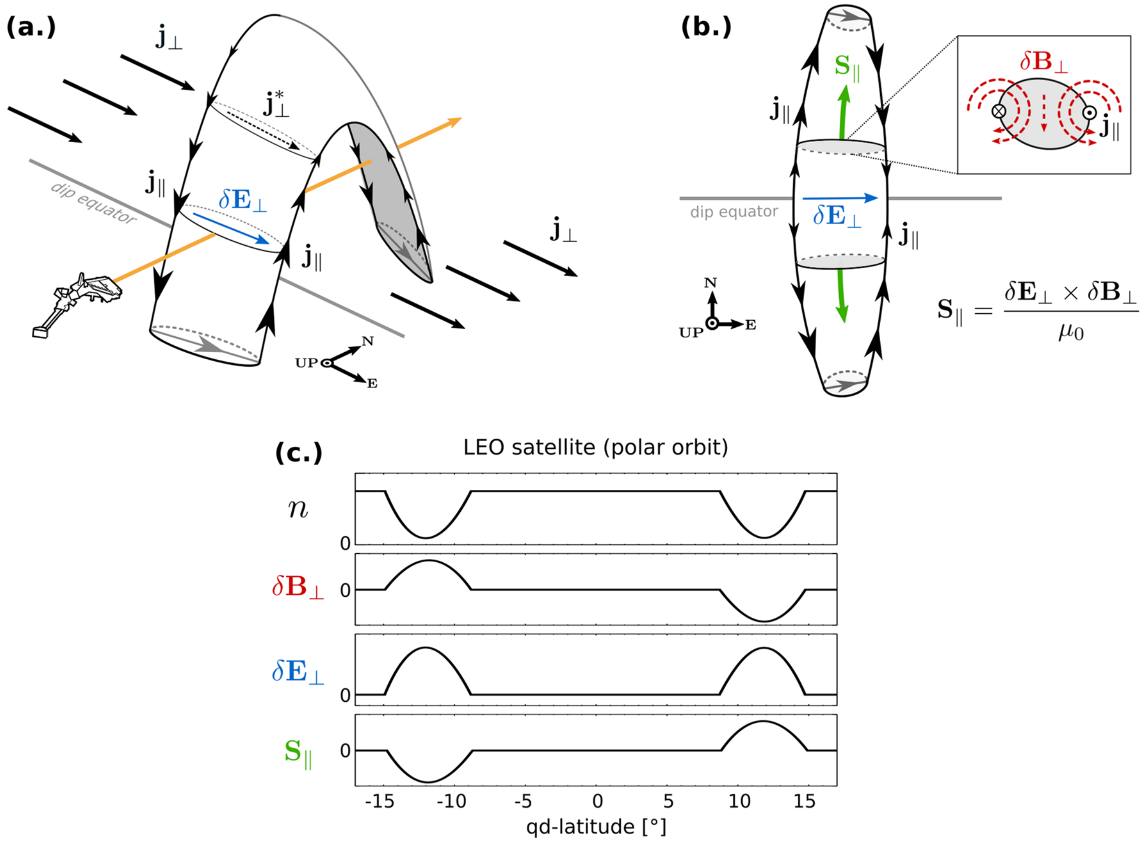

Fig. 1 **a** Depicts an equatorial plasma depletion (EPD) as a density-depleted magnetic flux tube intercepted from south to north by a polar-orbiting satellite. The sketch shows eastward zonal currents $\mathbf{j}_\perp$ diverging as field-aligned currents $\mathbf{j}_\parallel$ at the walls of the EPD. Weak zonal currents $\mathbf{j}^*_\perp$ are shown inside the depletions together with an eastward polarization electric field $\delta\mathbf{E}_\perp$. **b** Is a zenithal view of the flux tube in **a**. It additionally describes the Poynting flux $\mathbf{S}_\parallel$ directed away from the dip equator, and the magnetic field $\delta\mathbf{B}_\perp$ associated with the currents $\mathbf{j}_\parallel$ in the northern magnetic hemisphere. Panel (c) illustrates the expected plasma density n, disturbed magnetic field $\delta\mathbf{B}_\perp$, polarization electric field $\delta\mathbf{E}_\perp$, and associated Poynting flux $\mathbf{S}_\parallel$ observed by a polar-orbiting satellite intercepting an EPD—as in **a**

1979; Bhattacharyya and Burke 2000; Basu 2005), FACs flowing away from the dip equator at the western wall of EPDs and backward at the eastern walls—as panels a and b of Fig. 1 show. Similarly, field-aligned and vertical currents flow in the background ionosphere accordant with dynamo theory, wherein the winds in the *F* region act as the generator at night and the *E*-region conductivity on shared magnetic field lines as the load (Kelley 2009). In terms of EPDs-related magnetic perturbations seen by low-earth orbiting (LEO) satellites, the perpendicular component of the magnetic field $\delta\mathbf{B}_\perp$ associated with FACs should present a positive signature in the southern magnetic hemisphere and a negative signature in the north, assuming a dynamo source at the dip equator. Figure 1 depicts this scenario in panel c, following the trajectory of the polar-orbiting satellite in panel a. In this regard, however, Stolle et al. (2006) found a significant amount of events with opposite magnetic signatures suggesting FACs flowing antiparallel to the ones in Fig. 1. In a different study dedicated exclusively to the characteristics of EPD-related FACs, Park et al. (2009) observed that for most of the EPDs detected before 2100 LT, the orientation of the currents was in agreement with the assumption described in Fig. 1. As for EPDs with distinct FACs detected after 2100 LT, the authors mentioned the possible influence of the background westward zonal electric fields and/or the decay of EPDs occurring later at night—suggesting the currents to be driven by a higher altitude equatorial source. In a follow-up study, using about 5 years of data from the Swarm constellation mission, Rodríguez-Zuluaga and Stolle (2019) assessed the spatial and temporal characteristics of these FACs. The study shows either positive or negative magnetic fluctuations concurrently in both hemispheres when a polar-orbiting satellite crosses the same depleted flux tube. These observations suggest that EPD-related FACs are mainly interhemispheric at the satellite's altitude. When examining the global distribution of EPDs sorted by the orientation of their FACs, clear patterns organized by longitude and season are exhibited. Two eye-catching examples seen in their study are the high occurrence of EPDs with positive magnetic fluctuations in both hemispheres nearby the south Atlantic magnetic anomaly (SAA) and the occurrence of EPDs with the same positive magnetic perturbation all over the world during the June solstice.

The importance of EPD-related FACs in the context of this study has to do with their role on the field-aligned electromagnetic energy, as seen in Poynting's theorem. The parallel component of the Poynting vector is given by,

$$\mathbf{S}_{\parallel} = \frac{\delta \mathbf{E}_{\perp} \times \delta \mathbf{B}_{\perp}}{\mu_0}, \tag{1}$$

where $\delta \mathbf{E}_{\perp}$ is the EPDs' polarization electric field due to eastward background currents and $\delta \mathbf{B}_{\perp}$ the perturbation of the geomagnetic field with respect to the main field $\mathbf{B}_0$, which is associated with FACs at the walls of EPDs (Fig. 1b). Even though studies have addressed EPD-related FACs and electric fields using observations, they have been mostly carried out separately due to the scarcity of simultaneous measurements. As stated earlier, EPD-related FACs have been observed using in situ magnetic field measurements from satellites such as CHAMP (e.g., Stolle et al. 2006; Park et al. 2009), and Swarm (e.g., Rodríguez-Zuluaga and Stolle 2019). On the other hand, electric fields and plasma drift velocities inside plasma depletions have been observed by satellites like the Atmosphere Explorer AE-C (e.g., McClure et al. 1977), San Marco D (e.g., Aggson et al. 1992), ROCSAT-1 (e.g., Su et al. 2001), DMSP (e.g., Huang et al. 2010), C/NOFS (e.g., Burke et al. 2012), Swarm (e.g., Rodríguez-Zuluaga et al. 2017), and recently by ICON (e.g., Park et al. 2021). Simultaneous observations of electric and magnetic fields gathered by Swarm were used by Rodríguez-Zuluaga et al. (2017) to assess for the first time the orientation of the Poynting flux inside equatorial plasma depletions, EPDs. The study aimed to unveil whether the dynamo source or generator was located at the dip equator, as suggested by different studies (e.g., Burke 1979; Bhattacharyya and Burke 2000; Dao et al. 2013) and depicted in Fig. 1, panel b. With a few events, the authors showed evidence of a Poynting flux flowing unidirectionally from one hemisphere to another inside the same depleted flux tube at an altitude of ca. 450 km. This observation suggests a dynamo source off the dip equator and below the satellite's altitude.

In this study, we use an extended electric field data set measured by the Swarm constellation mission during topside equatorial spread *F* events. The measurements are combined with simultaneous magnetic field observations from the same spacecraft to compute the Poynting flux associated with the large-scale structure of the phenomenon. We address the effect of the plasma density, geographic location, season, and local time on the Poynting flux magnitude inside EPDs. With regard to the component of the Poynting flux due to the disruption of the background currents by topside spread *F*, we make use of the Cornell electrodynamics model to assess this phenomenon considering critical parameters in a three-dimensional ionosphere. Additionally, we suggest a possible explanation to previous observations of an off-equatorial dynamo source seen as interhemispheric flows at LEO altitudes.

Observations

The Swarm mission

The Swarm constellation is a satellite mission of the European Space Agency (ESA) dedicated to studying the Earth's magnetic field and its temporal evolution (Friis-Christensen et al. 2006; Olsen et al. 2013). It comprises three identical satellites named *Alpha*, *Charlie*, and *Bravo* launched on November 22, 2013 into near-polar, circular orbits. For most of the time in the last 8 years, *Alpha* and *Charlie* have flown side-by-side separated by about 1.4° in longitude at the equator, at 87.35° inclination angle and an altitude of ca. 470 km. *Bravo* has orbited at a higher initial altitude of 520 km and 87.75° inclination angle. As of the date of this paper, the altitude at the equator of *Alpha* and *Charlie* is about 438 km, and of *Bravo* of about 508 km. Each spacecraft uses an absolute scalar magnetometer (ASM) and a vector field magnetometer (VFM) to derive the absolute vector magnetic field. Detailed information on the calibration of the magnetic vector field measurements is given by Tøffner-Clausen et al. (2016). This study uses calibrated magnetic vector data at a 1-Hz rate. Apart from the ASM and VFM, each spacecraft is equipped with two Thermal Ion Imaging (TII) sensors—horizontal and vertical—and two Langmuir probes (LPs) to measure ionospheric drift (or flow) velocities ($\mathbf{V}_i$) and plasma density, respectively. Ionospheric electric fields $\mathbf{E}_{\perp}$ in the direction perpendicular to the geomagnetic field $\mathbf{B}_0$ are derived through the relation $\mathbf{E}_{\perp} = -\mathbf{V}_i \times \mathbf{B}_0$, as described by Knudsen et al. (2017). In the same study, the authors report on a transient, secondary signal to the primary ionospheric drift signal that appeared after the first weeks of Swarm operation, likely due to the presence of water in the sensors. As a result, the operation of the instrument has been limited to one to eight orbits per day. Since the electric field estimates are provided for both the horizontal and vertical TII sensors, and to decrease the impact of any possible

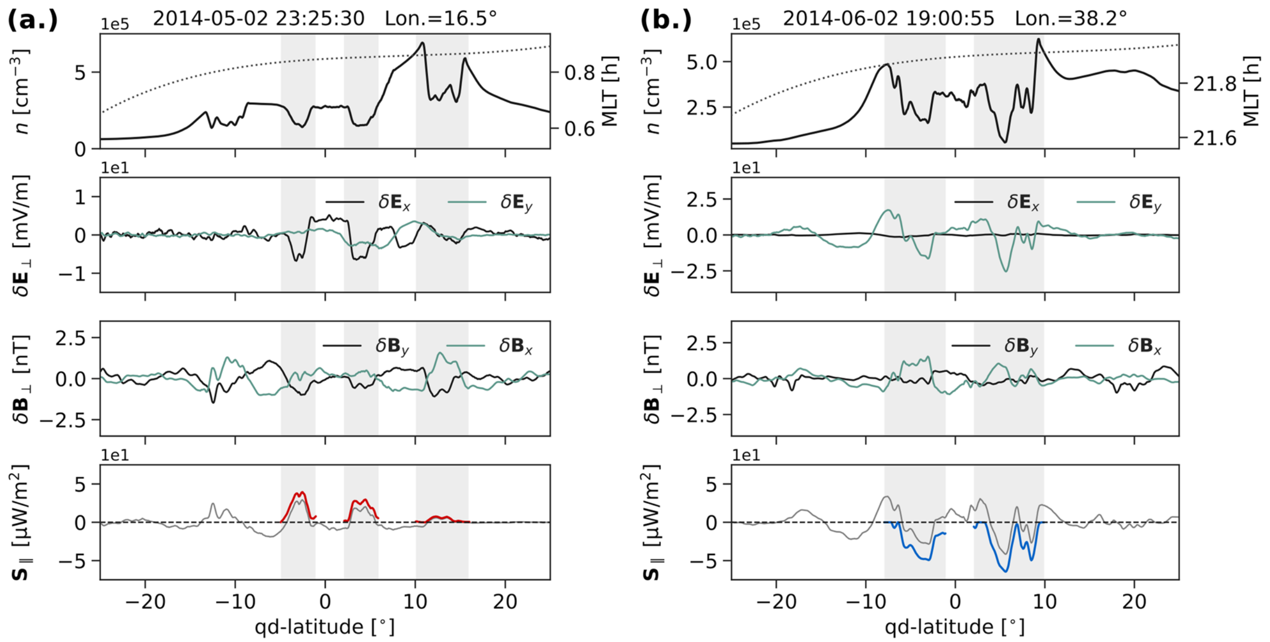

Fig. 2 Typical observations of EPDs by the Swarm satellites as a function of quasi-dipole latitude. From top to bottom, **a** and **b** present plasma density (n) and magnetic local time (MLT)—in the same panel, electric and magnetic field components perpendicular to the mean geomagnetic field ($\delta \mathbf{E}_\perp$, $\delta \mathbf{B}_\perp$), and field-aligned Poynting flux ($\mathbf{S}_\parallel$). **a** and **b** are observations from Swarm *Bravo* (ca. 520 km) and *Charlie* (ca. 470 km) describing examples of northward and southward Poynting flux, respectively. The gray line in the bottom panels is the Poynting flux computed with the measurements in the middle panels. After using a rolling ball algorithm, the red and blue lines are the final Poynting flux. The gray regions highlight flagged events used in the statistics—i.e., each gray region corresponds to a single point in the following scatter plots

overflow coming from a single sensor, we use the mean between the two sets of estimates. Drift velocity resolution has been estimated from flight data to be better than 0.5 mV/m (1 σ) for plasma densities greater than 10^4 cm^{-3}. This paper uses electric field data at a 1-Hz rate decimated from the original 2-Hz rate to coincide with the magnetic field observations. The plasma density corresponds to ion density also decimated to a 1-Hz rate.

EPDs detection and Poynting flux computation

The automatic detection of EPDs follows the methodology by Rodríguez-Zuluaga and Stolle (2019) using plasma density measurements between 18 and 06 magnetic local time. Distinctly in this study, the background plasma density n_0 is retrieved using a rolling ball algorithm over orbits within ±30° of quasi-dipole latitude. EPDs are defined as deviations of the plasma density n from the background n_0, i.e., $\delta n = n - n_0$. To flag EPDs we use δn deviations greater than 30% of the background density; i.e., $|\delta n / n_0| > 0.3$. Consecutive values of this kind are grouped in a single EPD if the distance between them is less than 450 km, i.e., ca. 60 s of orbit trajectory. A distance greater than or equal to 450 km between such variations represents the beginning of a new event. Examples of flagged EPDs are shown in Fig. 2 highlighted by gray bands. For every single EPD, a unique background density value n_0 synchronized with its minimum density value n_{min} is used to get the EPDs' depth δn; i.e., $n_0 - n_{\mathrm{min}}$. EPDs with a δn less than or equal to 10^4 cm^{-3} are discarded. We add 20 s at the beginning and the end of each EPD for every final flagged event, which serves as padding for correlations among different parameters later in the study. Figure 2 shows two Swarm passes during topside spread F events.

The electric and magnetic fields are defined in a mean-field aligned frame, where the z component is parallel to the main geomagnetic field pointing northward. The x component is confined to the magnetic meridian plane pointing toward higher magnetic L-shells, and the y direction completes the triad pointing eastward, i.e., $\hat{y} = \hat{z} \times \hat{x}$. To keep apart the magnetic field related to ionospheric currents, we remove from the measurements the components associated with the core, lithosphere, and magnetosphere using the CHAOS-7 geomagnetic field model (Finlay et al. 2020). To avoid Alfvénic contributions in the computation, we remove variations smaller than 100 km from all the measurements by using a second-order Savitzky-Golay filter with a 13 s window. We also remove variations greater than 2000 km from

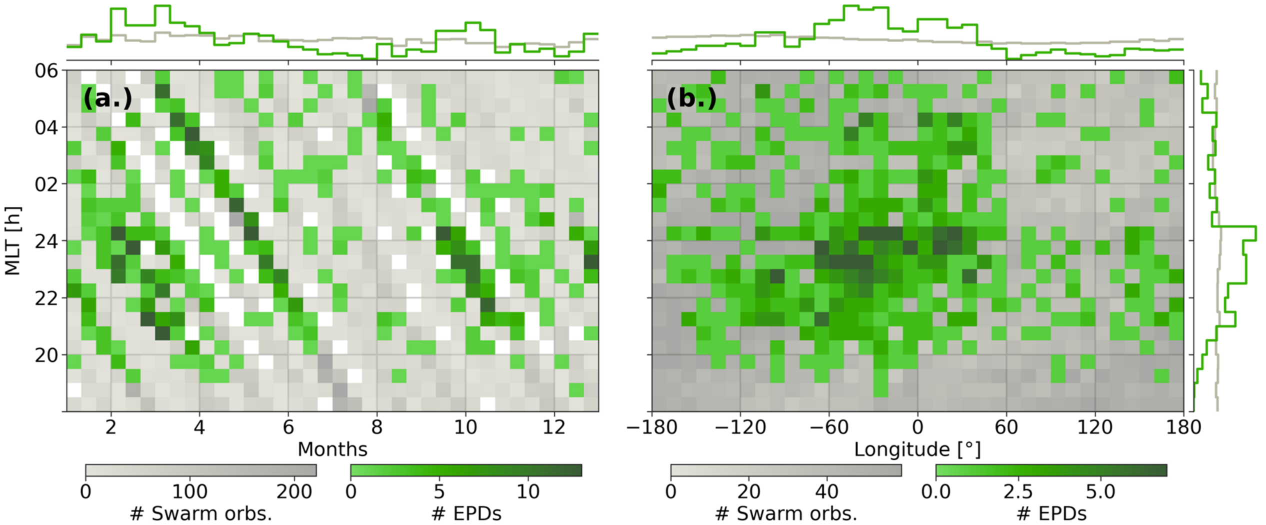

Fig. 3 **a** and **b** present in gray the number of Swarm orbits with available electric field data between 1800 and 0600 magnetic local time (MLT) from 10 January 2013 to 4 November 2021. In green are the number of equatorial plasma depletions (EPDs) used in this study. In **a**, the counts are organized by months with pixel dimensions of 10 days per 30 min. **b** shows the counts as a function of geographic longitude with pixel dimensions of 10° per 30 min. Histograms in gray and green on the top and on the right of the plots are for reference purposes

all the measurements using a 250 s window. The resulting electric and magnetic fields ($\delta\mathbf{E}_\perp$, $\delta\mathbf{B}_\perp$) are assumed to come mainly from plasma density perturbations (see Fig. 2, middle panels). It means no background electric fields (i.e., background ion drift velocities) and background currents are taken into account in the observational part of this study. We compute the Poynting flux by crossing the electric and magnetic fields. To minimize the effect of instrument noise that may occasionally dominate the Swarm TII data, only EPDs in which at least one pair of mutually perpendicular electric and magnetic field components are well correlated, are considered—i.e., the absolute value of the correlation coefficient |r| between $\delta\mathbf{E}_x$ and $\delta\mathbf{B}_y$, or $\delta\mathbf{E}_y$ and $\delta\mathbf{B}_x$ within an EPD must be greater than or equal to 0.6. Additionally, the resulting Poynting flux has to be also well linearly correlated with the plasma density ($|\mathrm{r}| \geq 0.6$). This last requirement is introduced to determine the orientation of the Poynting vector, such as a negative (positive) coefficient defines a positive (negative) vector—i.e., north (south) $\mathbf{S}_\parallel$ (see Fig. 1b and c). That latter step assumes unidirectional Poynting flux—it rejects EPDs that present antiparallel ion drifts within the depletion. Finally, we apply the same rolling ball average used to isolate the plasma density depletions as a guide to isolate the corresponding perturbations in Poynting flux. This procedure is performed over the flagged events only, i.e., gray regions in Fig. 2. The bottom panels of Fig. 2 show the final Poynting flux in thick color lines. The red (blue) color denotes northward (southward) fluxes. The mean energy flux of each event $|\overline{\mathbf{S}}_\parallel|$ is taken as an estimate of its magnitude, and it corresponds to the integrated Poynting flux along the EPD divided by the duration of the observation.

For reference, Fig. 3 shows the distribution in time and space of both the available electric field data from 10 January 2013 to 4 November 2021 and the number of EPD events included in this study. Panel a displays in gray the number of Swarm orbits with available data as a function of magnetic local time and month. In green, there is the number of flagged EPDs. Panel b follows the same lines of the panel a but as a function of geographic longitude. At first glance, it is noticed that most of the spread *F* events concentrate on both equinox periods. Regarding magnetic local time, the majority of detected EPDs are between 1800 and 2400 hours, likely due to the rejection of events with $|\delta n| \leq 10^4\ \mathrm{cm}^{-3}$ and $|\delta \mathrm{n}/\mathrm{n}_0| < 0.3$—which are typical of post-midnight hours. Concerning the longitudinal distribution, the more significant part of spread *F* detections is confined between – 70° and 40°, in agreement with the well-known seasonal variability of the phenomenon (e.g., Stolle et al. 2006; Xiong et al. 2010).

Characteristics of EPD-related Poynting flux

Figure 2 presents typical examples of topside spread *F* as seen by the Swarm spacecraft (*Bravo* and *Charlie* in panels a and b, respectively). The figure shows plasma density, electric fields, magnetic fields, and Poynting flux for two orbits in May and June 2014. The top panels display the magnetic local time (MLT) along the orbit in dotted lines. In both examples, the density depletions are

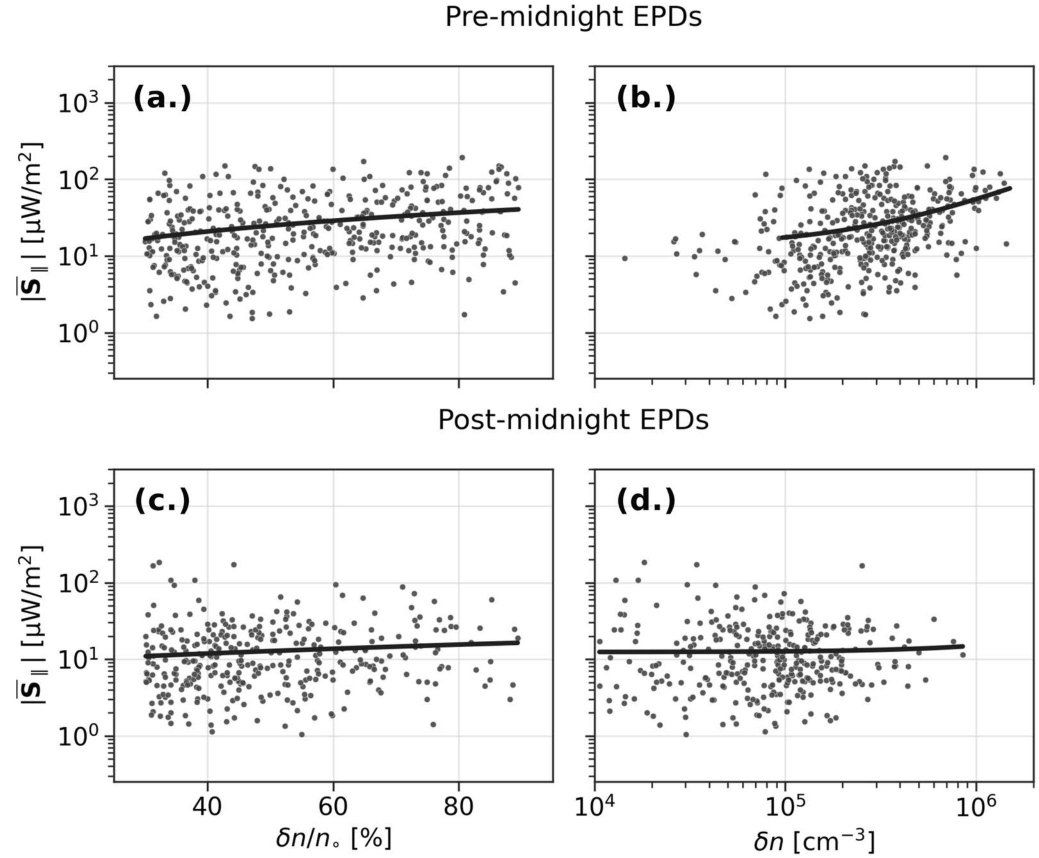

Fig. 4 The four panels show EPD-related mean Poynting flux $|\overline{\mathbf{S}}_{\parallel}|$ as a function of the depletions' depth relative to the background $\delta n/n_0$ in **a** and **c**, and depletions' depth δn in **b** and **d**. The rows indicate pre- and post-midnight EPDs

located at magnetically conjugate points. The small MLT variations along the orbit when intercepting the depletions suggest the satellites flew approximately along the same magnetic meridian, crossing the same density-depleted magnetic flux tube as depicted in Fig. 1a. In both examples, the Poynting flux indicates unidirectional flows from one hemisphere to the other, northward in red and southward in blue (panels a and b). When it comes to the electric and magnetic field measurements, we concentrate on the relative fields inside the depletions with respect to the ambient fields. Since the electric field data are derived from ion drift velocities, we only look at the relative velocity of the ions inside the depletion with respect to the ambient and not at the ambient plasma drift velocity itself. In Fig. 2a, only three out of four depletions are flagged. The first plasma depletion is not included in the statistics because no associated electric field perturbation is observed. The other three cases only have clear electric field signatures in the x component (vertical, positive upward), and almost no signature in the y component. That means the depletions are drifting vertically with the ambient plasma, or at least, no significant vertical ion drift velocity is observed inside the depletions relative to the ambient plasma drift. On the contrary, a considerable eastward zonal ion drift velocity in the two depletions nearby the dip equator is noted. At the same time, the farther north depletion shows signatures of both westward and eastward ion drift velocities inside. The magnetic field shows signatures in the three cases that suggest field-aligned currents flowing southward (northward) at the western (eastern) walls of the depletions (i.e., northward is in the direction of the mean geomagnetic field). Distinctly, the example in Fig. 2b displays almost no electric field variations in the x component but prominent westward zonal electric fields in both depletions. That means the EPDs are mainly drifting downward with respect to the ambient plasma. Regarding field-aligned currents, the magnetic field signatures inside EPDs suggest the same configuration as the one in panel a, that is, currents flowing southward (northward) at the western (eastern) walls of the depletions.

In Fig. 4, we assess the relation between EPDs plasma density (δn and $\delta n/n_0$), and the mean Poynting flux ($|\overline{\mathbf{S}}_{\parallel}|$). Each dot represents a single EPD event such as the

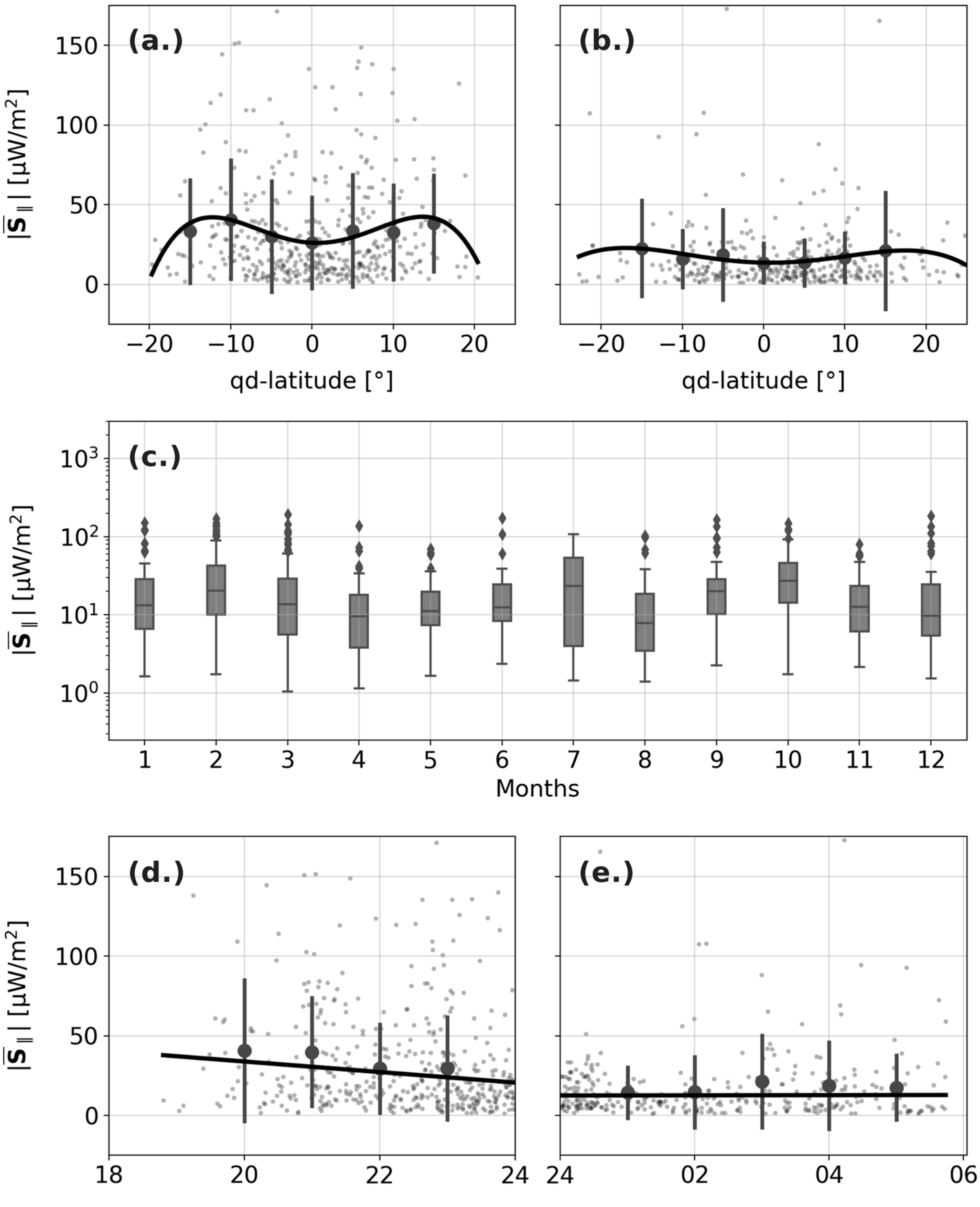

Fig. 5 Three rows display EPDs mean Poynting flux as a function of magnetic latitude for pre-midnight and post-midnight EPDs independently in **a** and **b**, monthly energy means in **c** and magnetic local time sorted by pre-midnight and post-midnight events in **d** and **e**, respectively

ones shaded in gray in Fig. 2. We sort the observations by magnetic local time between pre-midnight in panels a and b and post-midnight EPDs in panels c and d. By comparing panels b and d, the pre-midnight EPDs display larger depletion depths than post-midnight EPDs, with most of the values greater than approximately $10^5\,\mathrm{cm}^{-3}$. For pre-midnight EPDs, the Poynting flux magnitude varies more strongly with δn than with $\delta n/n_0$. In contrast, post-midnight EPDs which typically present values of $\delta n < 10^5\,\mathrm{cm}^{-3}$, show no relation between the depletion depth and the mean Poynting flux. Overall, both the absolute and relative depletion depth correlates poorly with the Poynting flux, with correlation coefficients of 0.27, 0.29, 0.13, and 0.04 corresponding to panels a–d, respectively.

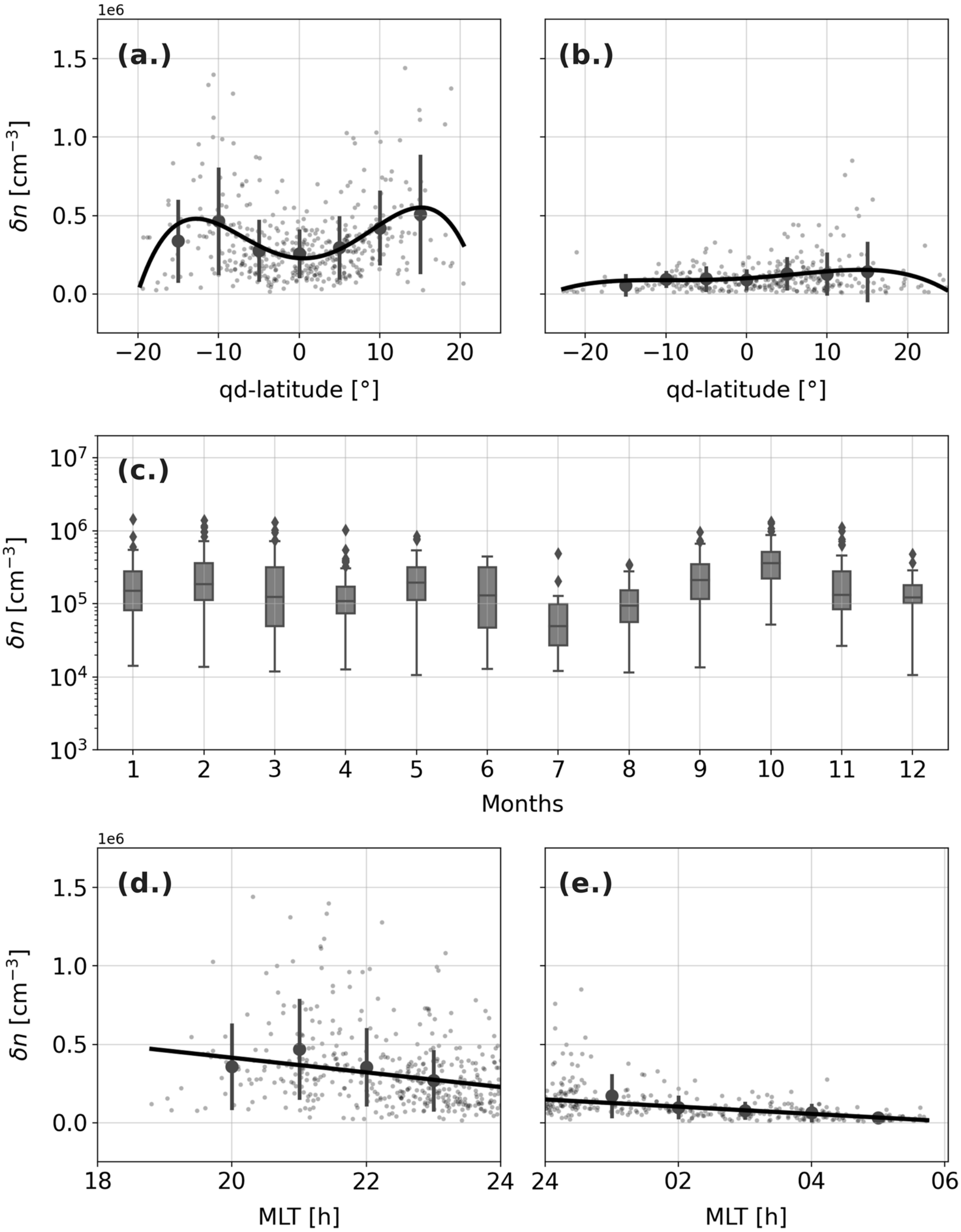

Fig. 6 Similar to Fig. 5, three rows show EPDs depth δn as a function of magnetic latitude for pre-midnight and post-midnight EPDs, **a** and **b**, monthly means in **c** and magnetic local time in **d** and **e**

Figure 5 depicts how the mean Poynting flux varies with magnetic latitude and time on a scale of months and hours. Regarding variations of the Poynting flux as a function of longitude (not shown in this paper), no preference for particular energy values is observed at specific longitudinal sectors. Panels a and b show EPDs mean Poynting flux as a function of quasi-dipole latitude for pre-midnight and post-midnight EPDs, respectively. A polynomial of degree four fits the data as a black-solid line and shows a tendency for lower Poynting flux values to occur mostly about the dip equator and higher values at about ±10°. This latitudinal feature, however, is evident during pre-midnight hours only. Panel c presents the mean Poynting flux for every single month together

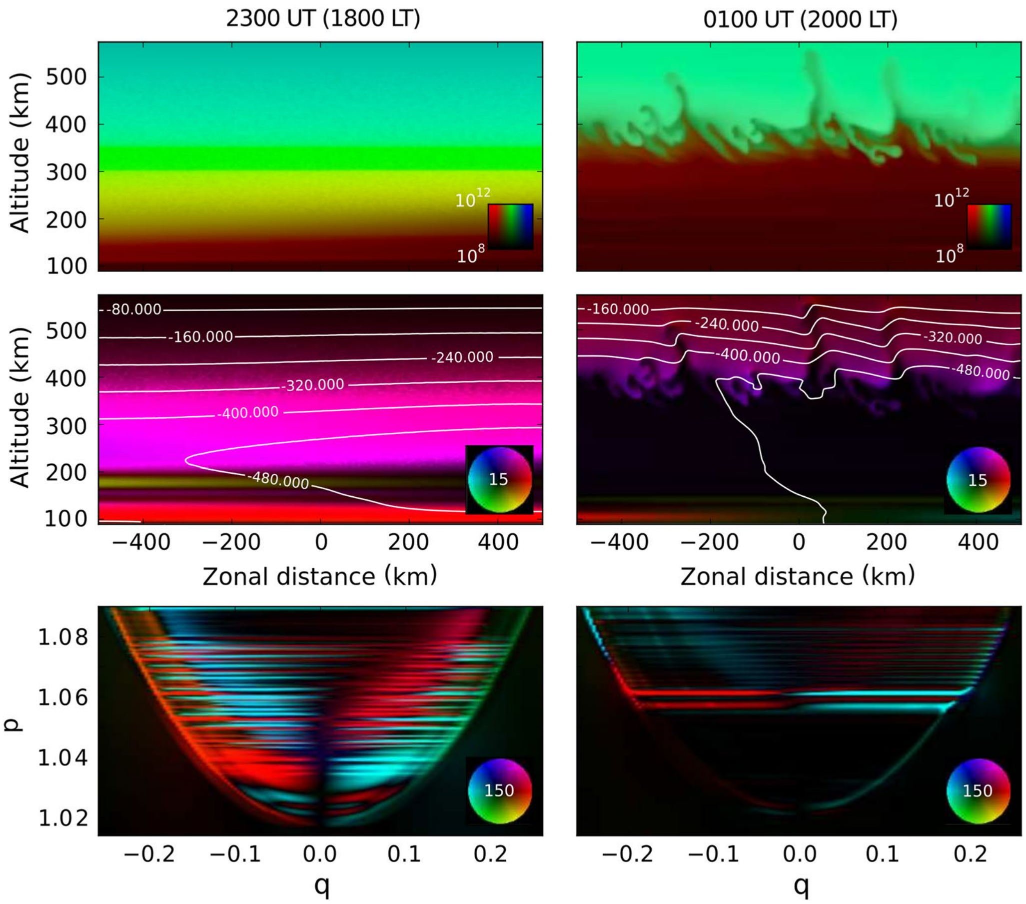

Fig. 7 Numerical simulation of convective instability in the Peruvian sector under equinox conditions. Columns at left and right depict conditions at 2300 UT and 0100 UT, respectively. The top panels depict ion number density in the equatorial plane, with red, green, and blue tones representing molecular ions, atomic oxygen ions, and hydrogen ions, respectively. The middle panels depict equipotential curves in the equatorial plane superimposed on vector current densities which can be interpreted using the color wheel. Full scale here is 15 nA/m^2. The bottom panels depict current density in the meridional plane. Full scale is 150 nA/m^2. The coordinates (p, q) used here and in subsequent figures refer to magnetic dipole coordinates, where p is the McIlwain L value and q parameterizes the displacement parallel to the field (e.g., Swisdak 2006). At the dip equator (i.e., $q = 0$), the p-values shown correspond to altitudes between approximately 100-575 km (as in the top and middle panels). At 100 km altitude, the q-values shown correspond to magnetic latitudes between ±15°. Lines of constant altitude are roughly parabolic in $p - q$ space

in one box plot. This plot shows the quartile values of the distribution along with extreme values. The middle line of the box represents the median, and the upper and lower lines, the upper and lower quartiles. The whiskers or lines extending parallel from the boxes reach points within 1.5 interquartile ranges from the lower and upper quartiles. The single dots are values that fall outside this range. In general, there is an oscillation of the mean Poynting flux values with peaks at about February, July, and October. The lowest values occur in April and August. Panels d and e of Fig. 5 present the mean Poynting flux as a function of magnetic local time for pre-midnight and post-midnight EPDs. The energy flux of pre-midnight EPDs slightly decreases with local time. This tendency seems to reach a minimum point at about 0100 MLT. After that time, its decreasing behavior vanishes.

Figure 6 presents the same structure as Fig. 5 but for EPD depth δn. In the pre-midnight sector, latitudinal variations of δn in panel a show lower values about the dip equator and larger values concentrated at about ±10°. EPDs depth does not show any particular latitudinal distribution in the post-midnight sector, except for larger values in the northern hemisphere. Panel c displays monthly values in single boxes. Higher values are seen in February, May, and around October. EPDs with the lowest depth occur around July. Panels d and e exhibit how EPDs depth decreases with time—as the plasma density decreases due to recombination.

Numerical simulations

The interpretation of Poynting flux measurements near equatorial plasma depletions is supported by numerical simulations of the ionospheric interchange instability. For this work, we use the Cornell electrodynamics model which has been described in a number of publications (e.g., Aveiro and Hysell 2010; Hysell et al. 2018, and references therein). The model combines a fully three-dimensional potential solver with a routine that updates the number density of four ion species (O^+, NO^+, O_2^+, and H^+) plus electrons in time. The effects of the Lorentz, pressure gradient, neutral drag, and gravitational forces are fully considered. Simulations are initialized using the output of the SAMI2-PE model which can reproduce *F*-region incoherent scatter measurements from the Jicamarca Radio Observatory closely (Huba et al. 2000; Varney et al. 2012). The Cornell model incorporates transport coefficients calculated with neutral atmospheric parameters taken from the NRLMSIS-00 model (Picone et al. 2002) and is forced using thermospheric wind estimates from the Horizontal Wind Model (HWM14) (Drob et al. 2015). The model is regional and it uses a tilted magnetic dipole geometry centered on the local magnetic equator at a specified longitude. The model is initialized with additive white noise.

We consider simulations in the Peruvian (76° W longitude) and African (20° E longitude) sectors during low solar flux, geomagnetically quiet conditions (F10.7 = 70, Ap = 15) around equinox, June, and December solstice. Simulations are initialized after local sunset and run forward in time for 2 hours. The background zonal electric field imposed on these simulations is taken from the Fejer Scherliess vertical drift model (Scherliess and Fejer 1999) only augmented artificially with a 15 m/s upward offset. This guaranteed the production of robust topside depletions within two hours in each of the cases considered.

Case 1 is for the Peruvian sector in equinox (day number 85). Fig. 7 shows selected simulation results upon initialization (2300 UT—left column) and two hours later (0100 UT—right column). At initialization, the current density in the equatorial plane is dominated by vertical currents associated with the *F*-region dynamo (Haerendel

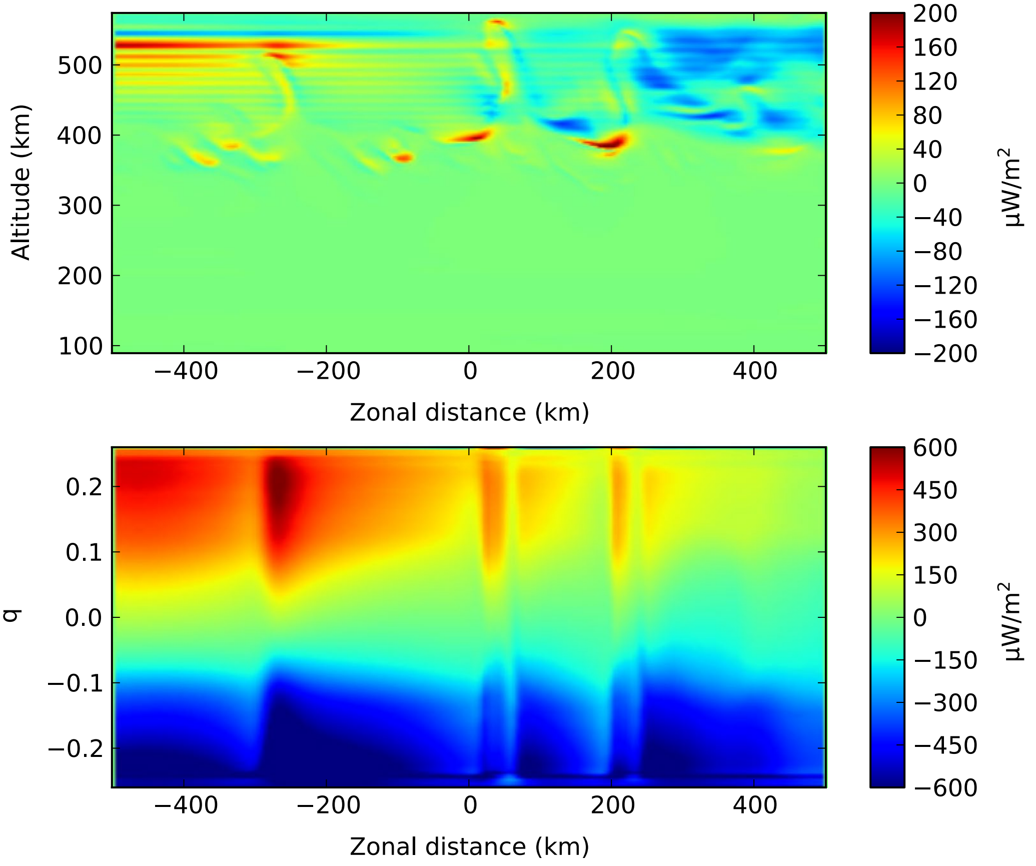

Fig. 8 Parallel Poynting flux in the equatorial plane (above) and on an *L*-shell with an apex altitude of 520 km (below) for the equinox simulation depicted in Fig. 7 at 0100 UT. Red (blue) tones denote northward (southward) fluxes. The *q*-values shown correspond to magnetic latitudes between ±15°

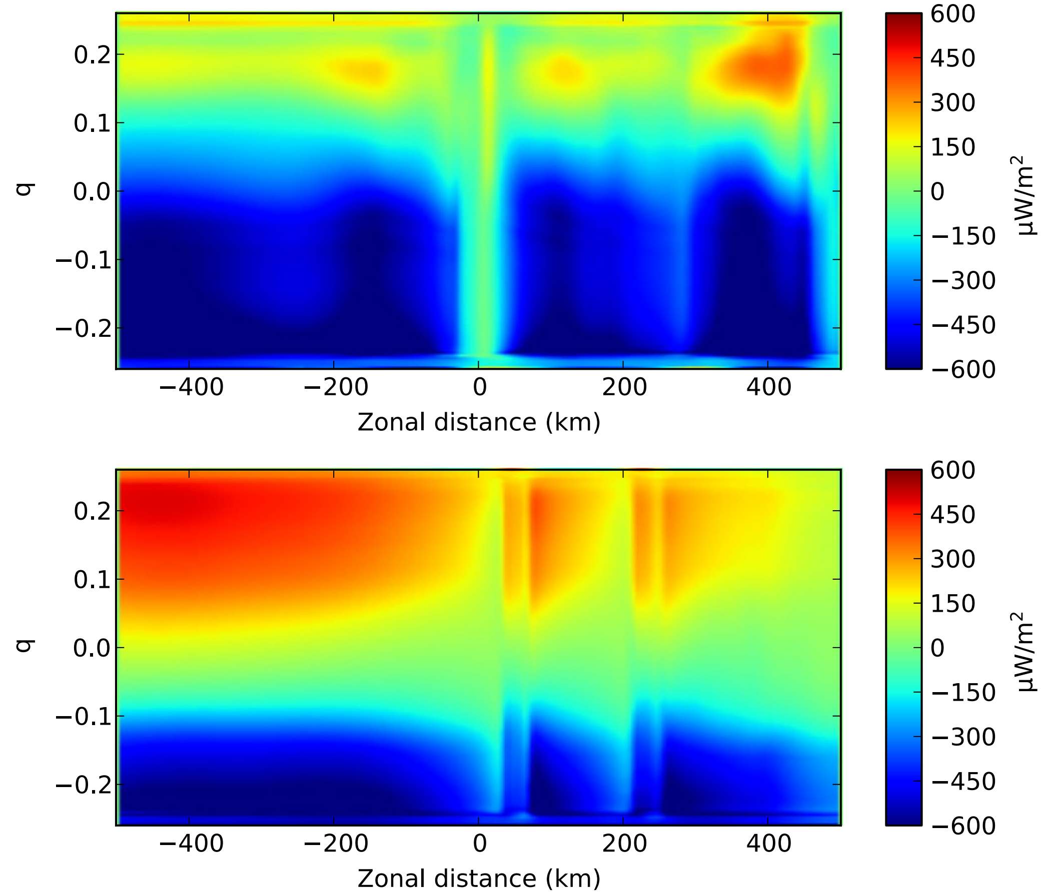

Fig. 9 Same as the lower panel of Fig. 8 except for December solstice (above) and June solstice (below)

et al. 1992; Maute and Richmond 2017). These currents close in the *E* region through field-aligned currents which are poleward (equatorward) on large (small) L-shells. The vertical currents drive fast-growing irregularities at the base of the *F* region which deform the bottomside where they can excite collisional interchange instability through a bootstrapping process (Hysell and Kudeki 2004; Hysell et al. 2020). The instability does not saturate, but instead mixes the *F* region through the production of plumes of plasma depletions that may penetrate into the topside (Zargham and Seyler 1989). The depletion plumes, in turn, interrupt and divert the pre-existing current distribution and the associated Poynting flux.

We compute the parallel component of the Poynting flux, $S_\| = (\mathbf{E} \times \mathbf{H}) \cdot \hat{b}$, where $\hat{b}$ is a unit vector parallel to the geomagnetic field. Focusing on perturbations to the Poynting flux, we consider $\mathbf{E} = \mathbf{E}_0 - \nabla\phi$ and neglect the explicit contribution from the imposed background zonal electric field $\mathbf{E}_0$. The dynamo electric field is part of $\nabla\phi$ in the simulation and so is retained. For the magnetic field **H**, we neglect the Earth's magnetic field and retain the magnetic field due to all ionospheric currents as prescribed by Ampere's law. In practice, we compute the magnetic vector potential by solving Poisson's equation and then proceed with the calculation of the perturbed magnetic field and the parallel Poynting flux. Field-aligned currents dominate other currents in the result.

The Poynting flux associated with the simulation in Fig. 7 for 0100 UT is shown in Fig. 8. The upper panel shows the Poynting flux at the magnetic equator, and the lower panel shows the Poynting flux on a fixed *L*-shell with an apex altitude of 520 km. Overall, Poynting flux flows mainly poleward in both hemispheres. This is consistent with dynamo theory wherein the winds in the *F* region act as the generator at night and the *E*-region conductivity on shared magnetic field lines as the load [(e.g., Kelley (2009)] The separatrix between northward and southward fluxes lies near the magnetic equator.

The Poynting flux is modified in the vicinity of plasma depletions. In the vicinity of the two high-altitude depletions in the eastern half of the simulation, the Poynting

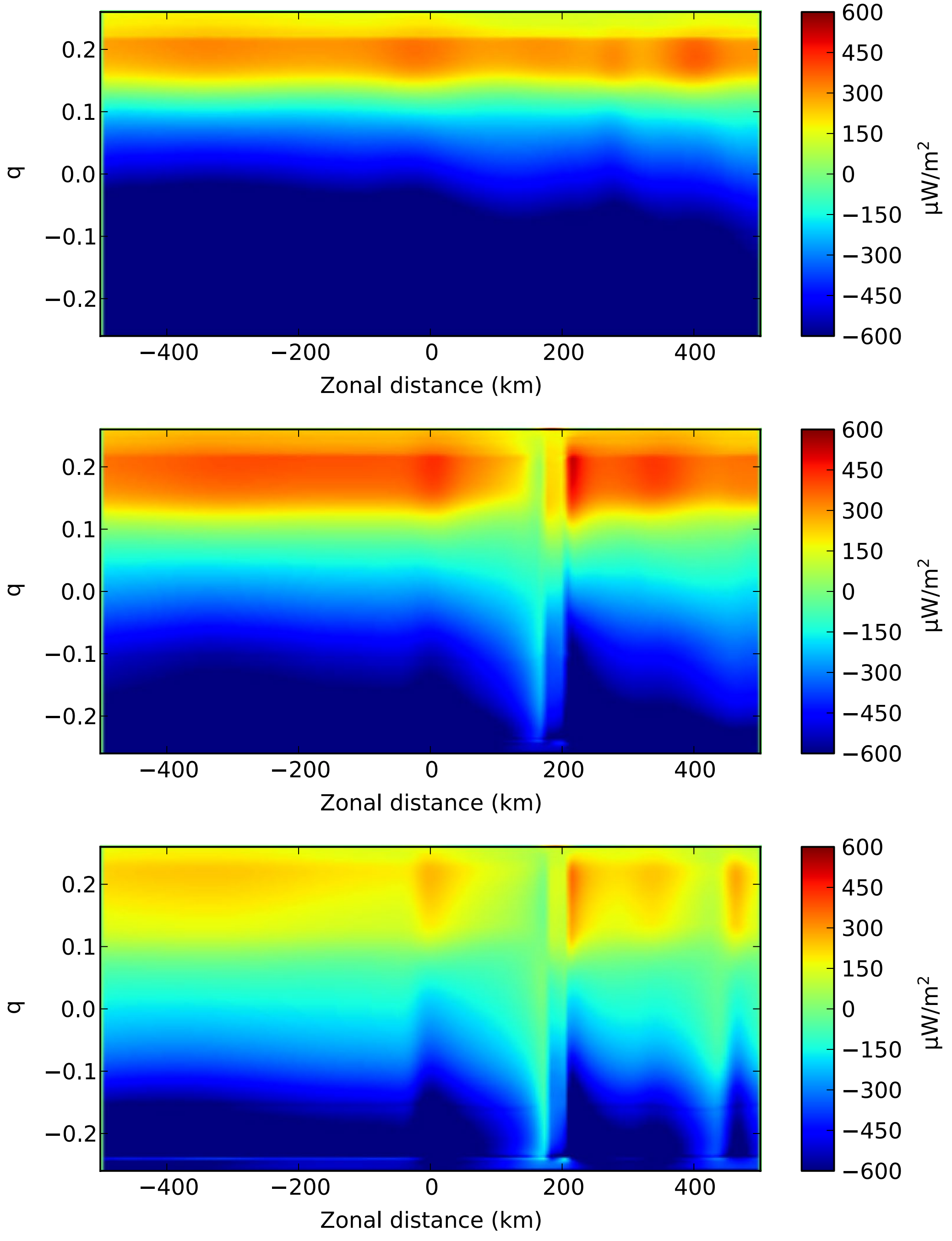

Fig. 10 Same as the lower panel in Fig. 8 except for the African sector and for December solstice (top), September equinox (middle), and June solstice (bottom)

flux at constant L value is reduced, enhanced, reduced, and enhanced, moving from west to east across each depletion. Above the lone plume in the westward half of the simulation, which was strictly below the constant-L surface in question here, the Poynting flux was simply reduced west of the plume and enhanced east of it.

Two more cases in the Peruvian sector were considered, with the results in Fig. 9. Here, the upper panel corresponds to December solstice (day 30), and the lower panel to post-equinox (day 100), approaching the June solstice. (Note that performing simulations closer to June solstice in the Peruvian sector is difficult because

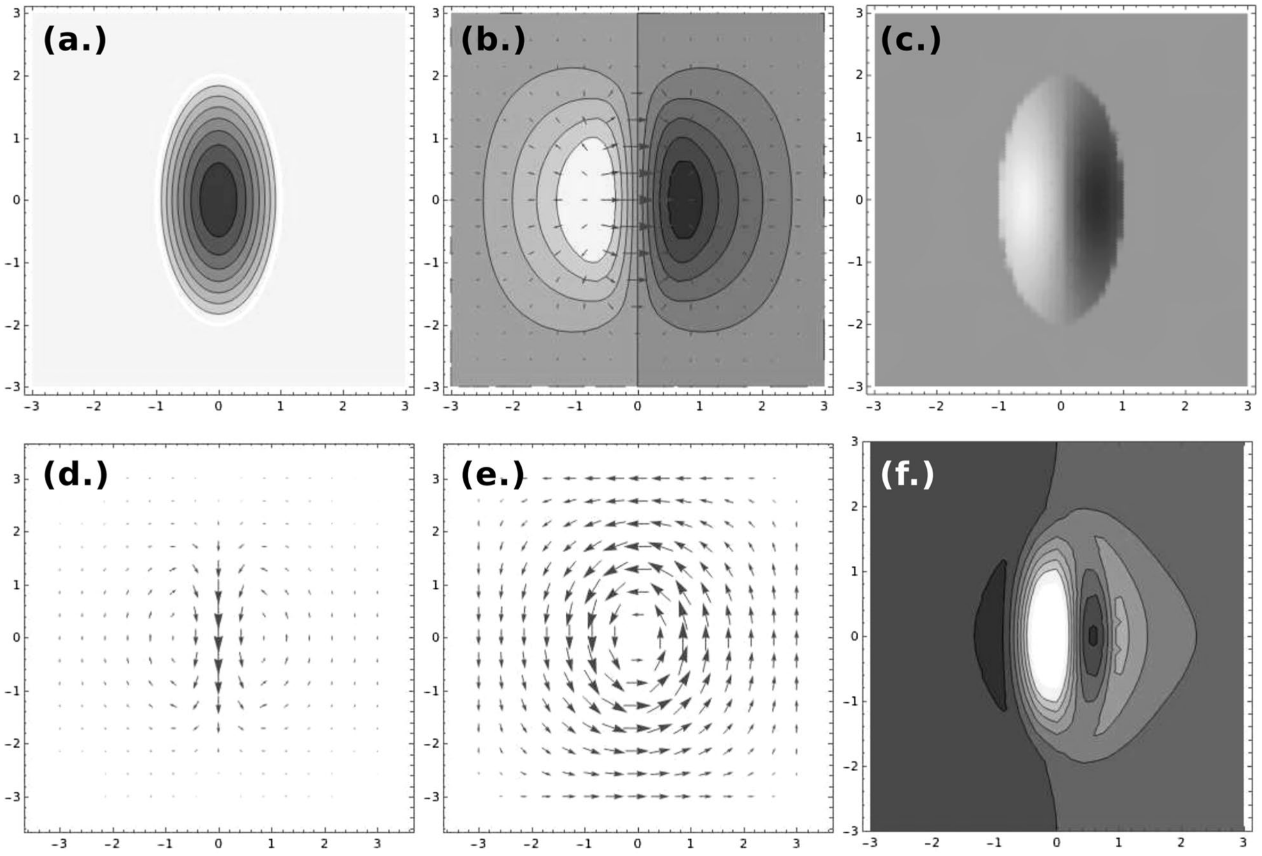

Fig. 11 Simplified model of parallel Poynting flux in vicinity of a plasma depletion. **a** Elliptical conductance depletion in plane perpendicular to the geomagnetic field. The plane perpendicular to B has a horizontal coordinate that runs magnetic east-west and vertical coordinate that is normal to the horizontal coordinate and to B. The scaling is arbitrary but determines the magnitudes of the fields. **a**–**c** are universal and do not depend on the hemisphere. Darker tones represent deeper depletion. The scaling is arbitrary. **b** Equipotential contours and electric field vectors representing the polarization of the depletion due to an eastern background current. Light (dark) tones represent positive (negative) potential. **c** Field-aligned current density antiproportional to the transverse Laplacian of the potential. Light (dark) tones represent poleward (equatorward) current density. **d** Magnetic field perturbations caused by the current density in **c** in the northern hemisphere. **e** Magnetic field perturbation caused by the interruption of the background northward field-aligned current density in the northern hemisphere. **f** Poynting flux perturbation in the northern hemisphere associated with a linear combination of **d** and **e**. Light (dark) tones represent positive (negative) perturbations in the northward flux

the ionosphere is very stable close to June solstice.) The seasonal effect is to shift the separatrix between northern and southern Poynting fluxes to the north and south, respectively, in December and June solstice. In fact, the shifts are due almost entirely to the winds prescribed by HWM14. In numerical tests, the separatrix could be moved northward or southward artificially by manipulating just the day number passed to the HWM14 model.

Simulation results for the African sector are shown in Fig. 10. From top to bottom, the figures represent the Poynting flux at 1900 UT, two hours after simulation initialization, for simulations corresponding to post-equinox (day 275), approaching December solstice, September equinox (day 258), and June solstice (day 115). (Note that performing simulations closer to December solstice in the African sector is difficult because the ionosphere is very stable then.) The results are comparable to those from the Peruvian sector except for a significant bias in the Poynting flux separatrix toward northern magnetic latitudes. Here, again, the bias was found to be attributable mainly to the HWM14 wind model. Conducting the simulations with neutral wind forcing prescribed by the model for the Peruvian sector largely eliminates the bias.

Reference Poynting flux model and interpretation

Perturbations in the Poynting flux in the vicinity of equatorial plasma depletions can be understood with some simplified, idealized modeling. Consider a Gaussian (elliptical) depletion in Pedersen conductance in the F region. The quasineutrality condition implies the following relationships between the background zonal electric field $\mathbf{E}_0$ and perturbed electrostatic potential ϕ (which are taken to be invariant along magnetic field lines), the hemispheric field-line integrated conductances in the E and F regions, Σ_F and Σ_E, and the parallel (poleward) current density at the base of the F region $J_\parallel$:

$$0 = \nabla_\perp \Sigma_F (\mathbf{E}_0 - \nabla_\perp \phi) - \Sigma_F \nabla_\perp^2 \phi + J_\parallel, \quad (2)$$

$$0 = \nabla_\perp \Sigma_F (\mathbf{E}_0 - \nabla_\perp \phi) - (\Sigma_F + \Sigma_E) \nabla_\perp^2 \phi, \quad (3)$$

where Eq. 2 involves integrating the quasineutrality from the magnetic apex point to the base of the F region, Eq. 3 from the apex point to the base of the E region, and where it is assumed that no parallel current flows at either the magnetic apex point or below the E region. Panel a of Fig. 11 is a depiction of Σ_F in the plane perpendicular to B. Panel b shows the corresponding solution to Eq. 3 in the form of equipotential lines and electric field lines. This is a nearly dipolar polarization electric field which will cause the original depletion to rise and deform.

Comparing Eq. 2 with Eq. 3 shows that $J_\parallel$ will be antiproportional to the Laplacian of the electrostatic potential. This parallel current density is shown in panel c and will be poleward on the west side of the depletion and equatorward on the east side. In addition, we must consider the effect of the depleted conductance on the background parallel current density driven by the F-region dynamo which it will interrupt. In the northern hemisphere, the interruption corresponds to an effective equatorward current proportional to the depletion in panel a leading to the perturbation in the magnetic field shown in panel e. (In practice, panels d and e are computed by solving Poisson's equation for the magnetic vector potential for the appropriate field-aligned current density perturbation).

Finally, the parallel Poynting flux in the northern hemisphere due to the electric field in b and a linear combination of the magnetic fields in d and e will exhibit the pattern shown in f. The contributions from d and e have odd and even symmetries, respectively, and the combination will be asymmetric with a net poleward Poynting flux perturbation. Along a horizontal cut through the vertical center of the pattern, the Poynting flux will be reduced, enhanced, reduced, and then enhanced, moving from west to east. In the southern hemisphere, the signs of the perturbations will be reversed from what is shown in the figure, but the pattern will remain that of reduction, enhancement, reduction, and enhancement of the background Poynting flux, moving from west to east. Just above the depletion, the pattern will exhibit reduction on the west side and enhancement on the east side. All together, the simple model can account for much of the behavior of the parallel Poynting in the vicinity of depletion plumes in the 3D simulations.

Analysis

The Poynting flux measurements show that the energy flux increases as the plasma density depletion's depth δn increases, only if $\delta n > 10^5\,\mathrm{cm}^{-3}$, which is typical for pre-midnight EPDs (see panel b, Fig. 4). In other words, δn and $|\overline{\mathbf{S}}_\parallel|$ are correlated only if the background plasma density n_0 is at least $10^5\,\mathrm{cm}^{-3}$. Smaller or shallow depletions typical of the post-midnight sector do not present any correlation between δn and $|\overline{\mathbf{S}}_\parallel|$. Because the plasma density in the F region is still prominent before midnight at low magnetic latitudes, zonal currents, especially those driven by gravity, are strong enough to feed field-aligned currents at the walls of EPDs. Due to current continuity, these zonal currents also contribute to polarization electric fields inside the EPDs. As the plasma density decays with time, the same is expected of the Poynting flux. Figure 5d and e show a subtle tendency for the Poynting flux to decrease with time until circa 0100 MLT. However, even though Fig. 6d and e display the same tendency for the EPDs depth, the plasma density keeps decreasing after 0100 MLT in the same fashion as before. Because of the direct relation between plasma density in the F region and field-aligned current density at the edges of EPDs, the lack of correlation between the Poynting flux and EPD depth after 0100 MLT might have to do with substantial variations of the zonal electric fields inside the depletions. Although these electric fields are mainly induced by background zonal currents in the F region, currents driven by background electric fields at lower altitudes can also play an important role. Due to the fact the electric field observations are derived from ion drift velocities, vertical winds might also contribute to these variations.

In a climatological analysis of the field-aligned currents (FACs) at the walls of plasma depletions, Rodríguez-Zuluaga and Stolle (2019) showed that at an altitude of about 450 km, the FACs flow from one magnetic hemisphere to the other. This means that a polar-orbiting satellite, like Swarm, only measures one of the two sets of FACs flowing at each side of the dynamo source—usually thought to be at the dip equator as depicted in Fig. 1. In other words, most of EPDs detected by Swarm in five years have shown a dynamo source or generator off the equator. Whether its location is in the northern or southern magnetic hemisphere can be deduced from the orientation of the FACs. Following the sketches in Fig. 1, if a polar-orbiting satellite crosses the same depletion as in panel a and detects positive magnetic perturbations in both hemispheres—like the one in the southern hemisphere in panel c—the FACs would flow southward (northward) at the western (eastern) wall of the EPD. Therefore, the dynamo source would be somewhere below the satellite in the northern hemisphere. Consequently, negative magnetic perturbations would imply the dynamo source in the southern hemisphere.

In Rodríguez-Zuluaga and Stolle (2019), the authors reported that the FACs' orientation presents a seasonal and longitudinal dependence. In June solstice, for instance, almost all EPDs detected show positive magnetic perturbations, suggesting a dynamo source in the northern hemisphere. The African sector presents an unstable ionosphere during this season, with the highest occurrence rate of EPDs worldwide. In Fig. 4 of the simulation section of this study, examples over the African sector show a preference for the dynamo source to be located in the northern hemisphere during June solstice and September equinox. Even though Rodríguez-Zuluaga and Stolle (2019) show that some EPDs present a generator in the southern hemisphere during September equinox, they are the minority and occur towards the dawn sector. However, in the Peruvian sector, the comparison between observations and simulations is not straightforward. The results in Rodríguez-Zuluaga and Stolle (2019) show that the Peruvian sector has a slightly higher preference for EPDs with a generator in the southern hemisphere during equinox and a prominent one during December solstice. Nevertheless, although the examples in Fig. 2 and the bottom panel of Fig. 3 (simulation section) show a subtle southward shift of the dynamo source, the example in Fig. 3, top panel, during December solstice, presents a northward generator.

An additional result in the study of Rodríguez-Zuluaga and Stolle (2019) is the correlation between the hemispherical asymmetry of the Pedersen conductance and the longitudinal and seasonal dependence of the FACs orientation. In terms of the position of the dynamo source, it generally occurs that the highest Pedersen conductance takes place in the opposite hemisphere. For instance, in the June solstice, the generator is located in the northern hemisphere. Since meridional winds generally blow from north to south during that season, the conductivity increases in the southern hemisphere as a response. In this paper, the simulations show that the shifts of the generator are due almost entirely to the winds prescribed by the HWM14 model, in agreement with the observations derived from the Swarm data.

Summary and conclusions

In this paper, we use observations of electric and magnetic fields from the Swarm mission to assess the Poynting flux near plasma density depletions associated with topside equatorial spread *F*. The detection of large-scale structures of the phenomenon commonly referred to as equatorial plasma depletions (EPDs) is based on in situ plasma density measurements from the same spacecraft. Here, we analyze the dependence of EPD Poynting flux on plasma density, local time, and geographic location of the EPDs detected. It has to be noted that only the Poynting flux inside the depletions is analyzed with observations. The electric field (derived from ion drift velocities) and magnetic fields are relative perturbations with respect to the background fields. The interpretation of the Poynting flux measurements is supported by numerical simulations using the Cornell electrodynamics model. The Poynting flux assessed through observations is associated with polarization electric fields inside EPDs and magnetic field perturbations related to field-aligned currents at the walls of the depletions. The numerical simulations, however, include—additionally—the magnetic field perturbation caused by the EPDs interruption of the field-aligned current density in the background ionosphere. The results of this study can be summarized as follows:

1. The Poynting flux is correlated with the plasma density, specifically, with the plasma depletion's depth. That is, the Poynting flux increases as the EPDs become more depleted. However, this feature is only observed when the background plasma density is at least 10^5 cm^{-3}, which is typical for the premidnight low latitude *F* region.
2. Since plasma density decays with time after dusk, both the Poynting flux and EPD depth decrease as well.
3. By picturing an EPD as a density-depleted magnetic flux tube (see Fig. 1), the Poynting flux is observed to increase with magnetic latitude along the tube, such that the energy is low at the dip equator and increases as it flows along the field lines towards higher latitudes. This characteristic is mainly due to the field-aligned currents at the edges of EPDs that increase with magnetic latitude.
4. Previous studies have suggested a dynamo source to be located at the dip equator, such that the Poynting flux must flow away from it, sinking into lower altitudes. However, our observations and simulations show a preference for an off-equatorial dynamo source. The unidirectional Poynting flux observed in a tube at about 450 km suggests a dynamo source below the satellite's altitude. On the other hand, the simulations show a separatrix between northward and southward fluxes lying mostly off the equator. It is proposed that neutral winds might play a relevant

role in this result. In the numerical simulations, the latitudinal shifts of the generator are due almost entirely to the winds prescribed by the HWM14 model. Besides, in an earlier study, Rodríguez-Zuluaga and Stolle (2019) suggest a connection between the generator's location and the hemispherical asymmetry of the conductance due to winds.

Acknowledgements
We thank the European Space Agency (ESA) for providing the Swarm data. The authors acknowledge the support from the International Space Science Institute (ISSI) through the international team "An Exploration of the Valley Region in the Low Latitude Ionosphere: Response to Forcing from Below and Above and Relevance to Space Weather."

Author contributions
JRZ and CS defined the study. JRZ processed the data. DH provided runs of numerical simulations. JRZ, CS, DH, and DJK interpreted the results. JRZ and DH wrote the manuscript. All authors read and approved the final manuscript.

Funding
This study has been supported through the Special Priority Programme (SPP) 1788 "DynamicEarth" of the German Research Foundation (DFG) under Grant Number STO 1074/3-1.

Availability of data and materials
The Level 1b data used and analyzed in this paper are available at ftp://swarm-diss.eo.esa.int.

Declarations

Competing interests
The authors declare that they have no competing interests.

Author details
[1]GFZ German Research Centre for Geosciences, Potsdam, Germany. [2]IAP Leibniz Institute of Atmospheric Physics at the University of Rostock, Kühlungsborn, Germany. [3]Cornell University, Ithaca, NY, USA. [4]University of Calgary, Calgary, AB, Canada.

Received: 5 April 2022 Accepted: 14 July 2022

References
Aggson TL, Burke WJ, Maynard NC, Hanson WB, Anderson PC, Slavin JA, Hoegy WR, Saba JL (1992) Equatorial bubbles updrafting at supersonic speeds. J Geophys Res Space Phys 97(A6):8581–8590

Aggson T, Maynard N, Hanson W, Saba J (1992) Electric field observations of equatorial bubbles. J Geophys Res Space Phys 97(A3):2997–3009

Aveiro H, Hysell D (2010) Three-dimensional numerical simulation of equatorial F region plasma irregularities with bottomside shear flow. J Geophys Res Space Phys. https://doi.org/10.1029/2010JA015602

Basu B (2005) Characteristics of electromagnetic Rayleigh-Taylor modes in nighttime equatorial plasma. J Geophys Res Space Phys. https://doi.org/10.1029/2004JA010659

Bhattacharyya A, Burke WJ (2000) A transmission line analogy for the development of equatorial ionospheric bubbles. J Geophys Res Space Phys 105(A11):24941–24950

Booker H, Wells H (1938) Scattering of radio waves by the F-region of the ionosphere. Terr Magn Atmos Electr 43(3):249–256

Burke WI (1979) Plasma bubbles near the dawn terminator in the topside ionosphere. Planet Space Sci 27(9):1187–1193

Burke WJ, Gentile LC, Shomo SR, Roddy PA, Pfaff RF (2012) Images of bottomside irregularities observed at topside altitudes. J Geophys Res Space Phys. https://doi.org/10.1029/2011JA017169

Dao E, Seyler C, Kelley M (2013) Three-dimensional modeling of the electromagnetic characteristics of equatorial plasma depletions. J Geophys Res Space Physics 118(6):3505–3514

Drob DP, Emmert JT, Meriwether JW, Makela JJ, Doornbos E, Conde M, Hernandez G, Noto J, Zawdie KA, McDonald SE, Huba JD, Klenzing JH (2015) An update to the Horizontal Wind Model (HWM): The quiet time thermosphere. Earth Space Sci 2(7):301–319

Fejer BG, Kelley M (1980) Ionospheric irregularities. Rev Geophys 18(2):401–454

Finlay CC, Kloss C, Olsen N, Hammer MD, Tøffner-Clausen L, Grayver A, Kuvshinov A (2020) The CHAOS-7 geomagnetic field model and observed changes in the South Atlantic Anomaly. Earth Planets Space 72(1):1–31

Friis-Christensen E, Lühr H, Hulot G (2006) Swarm: a constellation to study the Earth's magnetic field. Earth Planets Space 58(4):351–358

Haerendel G, Eccles J, Cakir S (1992) Theory for modeling the equatorial evening ionosphere and the origin of the shear in the horizontal plasma flow. J Geophys Res Space Phys 97(A2):1209–1223

Huang C-S, de La Beaujardiere O, Pfaff R, Retterer J, Roddy P, Hunton D, Su Y-J, Su S-Y, Rich F (2010) Zonal drift of plasma particles inside equatorial plasma bubbles and its relation to the zonal drift of the bubble structure. J Geophys Res Space Phys. https://doi.org/10.1029/2010JA015324

Huba J, Joyce G, Fedder J (2000) Sami2 is another model of the ionosphere (SAMI2): a new low-latitude ionosphere model. J Geophys Res Space Phys 105(A10):23035–23053

Hysell D (2000) An overview and synthesis of plasma irregularities in equatorial spread F. J Atmos Solar Terr Phys 62(12):1037–1056

Hysell D, Kudeki E (2004) Collisional shear instability in the equatorial F region ionosphere. J Geophys Res Space Phys. https://doi.org/10.1029/2004JB002998

Hysell D, Larsen M, Fritts D, Laughman B, Sulzer M (2018) Major upwelling and overturning in the mid-latitude F region ionosphere. Nat Commun 9(1):1–11

Hysell D, Rao S, Groves K, Larsen M (2020) Radar investigation of postsunset equatorial ionospheric instability over Kwajalein during project WINDY. J Geophys Res Space Phys 125(6):e2020JA027997

Kelley MC (2009) The Earth's ionosphere: plasma physics and electrodynamics, vol 96. Academic press, Cambridge

Knudsen D, Burchill J, Buchert S, Eriksson A, Gill R, Wahlund J-E, Åhlen L, Smith M, Moffat B (2017) Thermal ion imagers and Langmuir probes in the Swarm electric field instruments. J Geophys Res Space Phys 122(2):2655–2673

Lühr H, Maus S, Rother M, Cooke D (2002) First in-situ observation of nighttime F region currents with the CHAMP satellite. Geophys Res Lett. https://doi.org/10.1029/2001GL013845

Maute A, Richmond AD (2017) F-region dynamo simulations at low and mid-latitude. Space Sci Rev 206(1):471–493

McClure J, Hanson W, Hoffman J (1977) Plasma bubbles and irregularities in the equatorial ionosphere. J Geophys Res 82(19):2650–2656

Olsen N, Friis-Christensen E, Floberghagen R, Alken P, Beggan CD, Chulliat A, Doornbos E, Da Encarnação JT, Hamilton B, Hulot G et al (2013) The Swarm satellite constellation application and research facility (SCARF) and Swarm data products. Earth Planets Space 65(11):1

Park J, Heelis R, Chao CK (2021) Ion velocity and temperature variation around topside nighttime irregularities: contrast between low-and mid-latitude regions. J Geophys Res Space Phys 126(2):e2020JA028810

Park J, Lühr H, Stolle C, Rother M, Min K, Michaelis I (2009) The characteristics of field-aligned currents associated with equatorial plasma bubbles as observed by the CHAMP satellite. Ann Geophys 27:2685–2697

Picone J, Hedin A, Drob DP, Aikin A (2002) NRLMSISE-00 empirical model of the atmosphere: statistical comparisons and scientific issues. J Geophys Res Space Phys. https://doi.org/10.1029/2002JA009430

Rodríguez-Zuluaga J, Stolle C (2019) Interhemispheric field-aligned currents at the edges of equatorial plasma depletions. Sci Rep 9(1):1233

Rodríguez-Zuluaga J, Stolle C, Park J (2017) On the direction of the Poynting flux associated with equatorial plasma depletions as derived from Swarm. Geophys Res Lett 44(12):5884–5891

Scherliess L, Fejer BG (1999) Radar and satellite global equatorial F region vertical drift model. J Geophys Res Space Physics 104(A4):6829–6842

Stolle C, Lühr H, Rother M, Balasis G (2006) Magnetic signatures of equatorial spread F as observed by the CHAMP satellite. J Geophys Res Space Phys. https://doi.org/10.1029/2005JA011184
Su S-Y, Yeh H, Heelis R (2001) ROCSAT 1 ionospheric plasma and electrodynamics instrument observations of equatorial spread F: an early transitional scale result. J Geophys Res Space Phys 106(A12):29153–29159
Swisdak M (2006) Notes on the dipole coordinate system. Physics. https://doi.org/10.48550/arXiv.physics/0606044
Tøffner-Clausen L, Lesur V, Olsen N, Finlay CC (2016) In-flight scalar calibration and characterisation of the Swarm magnetometry package. Earth Planets Space 68(1):129
Varney R, Swartz W, Hysell D, Huba J (2012) SAMI2-PE: a model of the ionosphere including multistream interhemispheric photoelectron transport. J Geophys Res Space Phys. https://doi.org/10.1029/2011JA017280
Woodman R (2009) Spread F—an old equatorial aeronomy problem finally resolved? Ann Geophys 27(5):1915–1934
Xiong C, Park J, Lühr H, Stolle C, Ma SY (2010) Comparing plasma bubble occurrence rates at CHAMP and GRACE altitudes during high and low solar activity. Ann Geophys 28(9):1647–1658
Zargham S, Seyler C (1989) Collisional and inertial dynamics of the ionospheric interchange instability. J Geophys Res Space Phys 94(A7):9009–9027

Publisher's Note